Engineering 4D seismic monitoring: A data-driven blueprint from the Devine hydrogen test site

Andrey Bakulin[1], Sujith Swaminadhan[1], Roy Burnstad[1], Jacob Badger[2], Mark Shuster[1], Mojdeh Delshad[3], and Muhammad Alhotan[3]

https://doi.org/10.1190/tle44100778.1

Abstract

We present a data-driven blueprint for engineering 4D seismic monitoring by integrating ultra-dense 3D surface seismic and vertical seismic profile (VSP) data at the Devine hydrogen test site with full-waveform modeling of 4D responses from reservoir simulations. Seismic data across a wide fold range (1–1600) are mined to quantify signal-to-noise ratio (S/N) and repeatability (normalized root mean square [NRMS]), producing fold versus quality curves and maps with quantified uncertainty. This transforms 4D survey design from guesswork into a structured engineering process. The shallow, weakly reflective Olmos target requires higher fold for reliable plume detection. Spatial S/N maps also reveal site-specific near-surface "thumbprints," areas with degraded S/N and elevated NRMS due to shallow heterogeneity, that must be empirically mapped to enable robust 4D strategies. We establish a quantitative design framework by linking NRMS, S/N, and acquisition parameters through the standard acquisition equation, forming a modern "box test" for 4D feasibility. Applying this blueprint to the upcoming hydrogen injection shows that small volumes (approximately 2 tons) of hydrogen, a highly responsive seismic tracer, can be tracked via distributed acoustic sensing (DAS) VSP, crosswell DAS, and surface seismic. Full-waveform modeling confirms strong 4D signatures across all methods, with crosswell DAS offering unmatched spatial resolution for imaging plume geometry and saturation. This integrated workflow, grounded in field data and modeling, delivers a transparent, reproducible foundation for 4D survey design. As Devine becomes a shared hydrogen injection testbed for academia and industry, it provides a unique platform for benchmarking monitoring technologies under controlled conditions, accelerating innovation and public trust in subsurface energy solutions.

Introduction

As geophysicists, we have long worked alongside geologists and drillers, with seismic imaging often serving as the only viable tool for mapping subsurface structures in exploration and gas storage. Today, seismic monitoring strengthens our role even further, positioning geophysics at the core of subsurface teams responsible for managing injection and production throughout the life of a field.

Despite success in marine 4D (Calvert, 2005; Johnston, 2013), land monitoring is less common, even with lower acquisition costs, due to higher risks from near-surface variability. No robust framework exists to manage this risk for 4D monitoring, particularly for repeatability in reservoir-scale monitoring. Consequently, land 4D projects are often inconsistent, lacking standardization and transferable lessons. Susan Hovorka, a CO_2 sequestration expert, called this the "giraffe spot picking game" (personal communication, 2024), as the same 4D data set yields varying anomalies depending on the geophysicist. This reflects high uncertainty and a lack of defensible standards, which are critical for trust from industry, regulators, and the public in carbon capture and storage (CCS) contexts.

Recently, sparse monitoring has become the buzzword for energy transition applications, often due to cost constraints rather than understanding technical risks. Ultimately, managing risks is crucial for optimizing oil and gas production, gas storage, or CCS containment to protect project economics and public safety.

While every subsurface case study yields unique insights, there should also be overarching lessons, clear methods, and measurable criteria for defining monitoring success. It is time to evolve 4D geophysics from an exciting craft into an engineering process, one where geophysicists clearly communicate trade-offs in terms understandable to both reservoir engineers and the public, enabling sound technical and economic decisions.

The ad hoc era of "Here's the budget, go do your best 4D" is no longer sustainable. It diffuses accountability and obscures the real value of geophysical input. Geophysicists may say, "We could've done better with more funding," while engineers respond, "You said we'd be fine, but you never explained what exactly we'd gain in monitoring performance for each additional dollar." That disconnect must be closed. What is needed is a technical framework that connects acquisition design parameters like trace density, fold, and source effort to monitoring objectives and associated costs.

In this study, we outline a practical methodology for 4D survey design using data-driven diagnostics applied to 3D surface seismic and VSP data from the Devine test site, which is slated for hydrogen injection testing. We show that managing overburden and near-surface complexity is key, and we demonstrate how a well-designed characterization survey enables deep mining of 4D risk quantitatively. This lays the foundation for deliberate, informed design, whether for surface seismic, VSP, or crosswell monitoring.

This paper has two goals. First, we present a data-driven 4D monitoring design workflow grounded in real data from the Devine test site, integrating ultra-dense 3D seismic, VSP, and full-waveform modeling to assess site-specific feasibility. Second,

---

Manuscript received 29 May 2025; accepted 27 June 2025.

[1] University of Texas at Austin, Bureau of Economic Geology, Austin, Texas, USA. E-mail: andrey.bakulin@beg.utexas.edu; sujith.swaminadhan@utexas.edu; roy.burnstad@beg.utexas.edu; jbadgerbsasn@gmail.com; mark.shuster@beg.utexas.edu.
[2] Formerly University of Texas at Austin, Bureau of Economic Geology, Austin, Texas, USA; presently FrequenSol LLC, Austin, Texas, USA. E-mail: jacob.badger@frequensol.com.
[2] University of Texas at Austin, Hildebrand Department of Petroleum and Geosystems Engineering, Austin, Texas, USA. E-mail: delshad@mail.utexas.edu; hotan@utexas.edu

we introduce the upcoming hydrogen injection experiment as part of the Bureau of Economic Geology's vision to establish Devine as a shared R&D platform where industry and academia can collaboratively test and advance monitoring technologies under controlled conditions. The site offers a real-world sandbox for developing reproducible and transferable 4D workflows.

Testbed for injection monitoring

The Devine test site, southwest of San Antonio, Texas, is a premier geophysical research facility operated by the Bureau of Economic Geology (BEG) at The University of Texas at Austin (Hardage, 1999, 2004). Originally donated by bp (then British Petroleum), the site has evolved into a state-of-the-art field lab for subsurface experimentation. It offers rare infrastructure and data access: five deep steel- and fiberglass-cased boreholes (to 3000 ft), shallow shot holes, and a rich archive of seismic, VSP, crosswell, and log data sets (Figure 1a). The site is uniquely suited for research at the intersection of geophysics, reservoir engineering, and environmental monitoring.

Led by GeoH2 (GeoH2, n.d.) and TCCS (TCCS, n.d.), the next phase centers on a planned hydrogen injection experiment, part of BEG's broader initiative to advance injection monitoring for energy transition applications. This test will target the Olmos Sandstone, a shallow (approximately 1600 ft), high-porosity formation. Lacking a structural trap (Devine test site, n.d.; Hosseini and Nicot, 2016), it offers an ideal environment to study capillary trapping and unconfined gas migration under realistic, low-risk conditions. Several tons of hydrogen will be injected into the aquifer, with no planned withdrawal, allowing monitoring to focus on containment, upward migration, and redistribution.

To support this, BEG is deploying two new wells, an injector and a monitor (Figure 1a), each equipped with fiber-optic sensors (DAS for acoustics, DTS for temperature, and DSS for strain, Figures 1c and 1d) and electrical resistivity tomography arrays (Figure 1e). These multiphysics sensors will enable high-resolution, time-lapse monitoring of plume evolution across seismic, thermal, strain, and electrical domains.

This paper outlines 4D monitoring feasibility at Devine, structured around a full signal-versus-noise workflow:

- Reservoir simulations predict plume evolution and elastic changes.
- New 3D seismic and VSP data are analyzed for imaging quality and 4D noise.
- Advanced finite-element waveform modeling (FEM) simulates 4D signal response and benchmarks it against simpler convolutional modeling.
- Feasibility is assessed by comparing modeled 4D signal to empirical 4D noise.
- Crosswell DAS modeling is introduced to track fine plume dynamics in this shallow setting, using two closely spaced wells.

The Devine site thus serves not only as a testbed for hydrogen injection but also as a shared platform where industry,

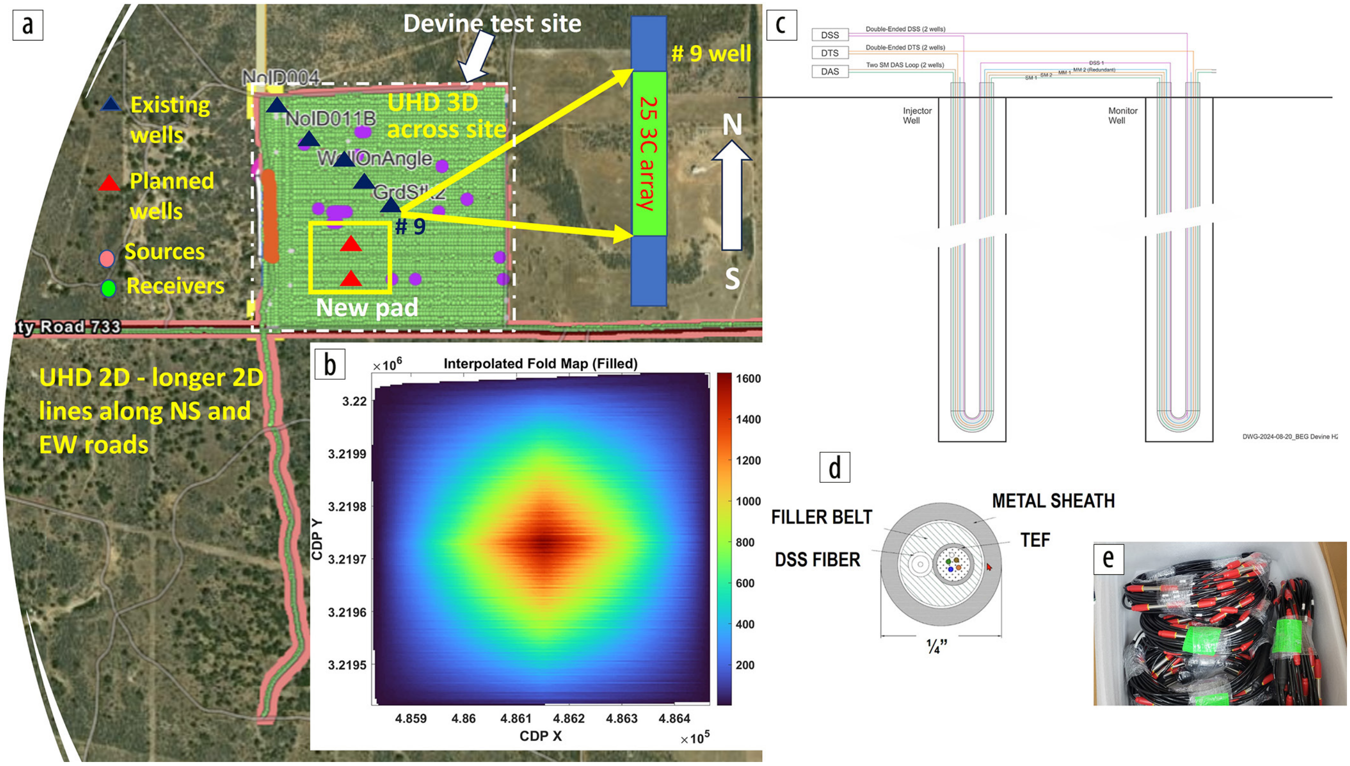

Figure 1. Layout of the Devine test site and experimental setup: (a) Site map showing existing and planned well locations overlaid with the ultra-dense 3D and 2D nodal seismic surveys, along with the 3D VSP acquired in existing well #9. (b) Fold map from the ultra-high-density 3D nodal survey, highlighting variable fold associated with fixed patch geometry. (c) Proposed instrumentation scheme for the new injection and monitoring wells, featuring behind-casing fiber-optic (DAS/DTS/DSS) and ERT arrays, both connected via a continuous fiber loop. (d) Fiber-optic cable selected for deployment. (e) ERT cable prepared for installation. All instrumentation is designed for permanent, behind-casing deployment.

academia, and service providers can collaboratively develop, test, and validate new monitoring technologies in a well-characterized environment.

Plume simulation and elastic property changes

To support monitoring design, we begin with reservoir simulations using Computer Modeling Group's GEM simulator (CMG-GEM) to evaluate the spatial and temporal evolution of the hydrogen plume and to quantify associated changes in elastic properties relevant for time-lapse detection. These simulations build on prior experience modeling hydrogen storage and analyzing sensitivity to reservoir and fluid properties (Alhotan et al., 2023a; Alhotan et al., 2023b; Machado et al., 2024).

The simulations target the Olmos Sandstone, a high-porosity (~30%), moderate-permeability (~100 mD) formation located at ~1600 ft depth with a thickness of ~50 ft (Figure 2e). A total of 2 tons of hydrogen is injected into the lower third of the reservoir, with no planned withdrawal. This setup enables focused assessment of buoyancy-driven migration, capillary trapping, and long-term redistribution behavior.

Big-picture plume behavior. Figures 2a–2d show an updip cross section from the 3D simulation, illustrating plume development over time. The hydrogen plume is fast moving, it ascends rapidly and reaches the top of the reservoir within one month, then spreads laterally to form a near-cylindrical body approximately 100 ft in diameter. This behavior is driven by the combination of relatively low injected volume and moderately high vertical permeability (Kv/Kh ≈ 0.5), supported by whole-core observations of burrowed textures. Saturation changes also evolve quickly: as hydrogen redistributes over time, saturation levels decrease progressively. An updip tongue forms just beneath the caprock, with a vertical thickness of approximately one model cell (~1 ft), as shown in Figure 2c.

Detailed plume evolution at well locations. Figures 2f–2g show vertical saturation and velocity profiles at the injector and a monitor well located 40 ft updip. Hydrogen reaches the offset well within 2–3 days, demonstrating rapid lateral transport. By one month, the plume ascends to the top of the formation (Figures 2b and 2f). Saturation initially peaks around 70% along the injector well but begins to decline after one month as the updip tongue develops (Figure 2f), eventually decreasing to ~40% by one year due to redistribution and capillary trapping. This stabilization phase defines a practical monitoring window, during which elastic changes are strongest and most localized.

Elastic changes and detectability. The corresponding compressional velocity reductions (ΔV_P), modeled using Gassmann's equations, track the plume's saturation evolution. Maximum ΔV_P values reach ~370 m/s at moderate hydrogen saturations (~8%), after which the response flattens across the 20%–80% saturation range due to the near-linear behavior of V_P under homogeneous saturation conditions. As a result, elastic contrast is strongest during early plume invasion, while later redistribution produces

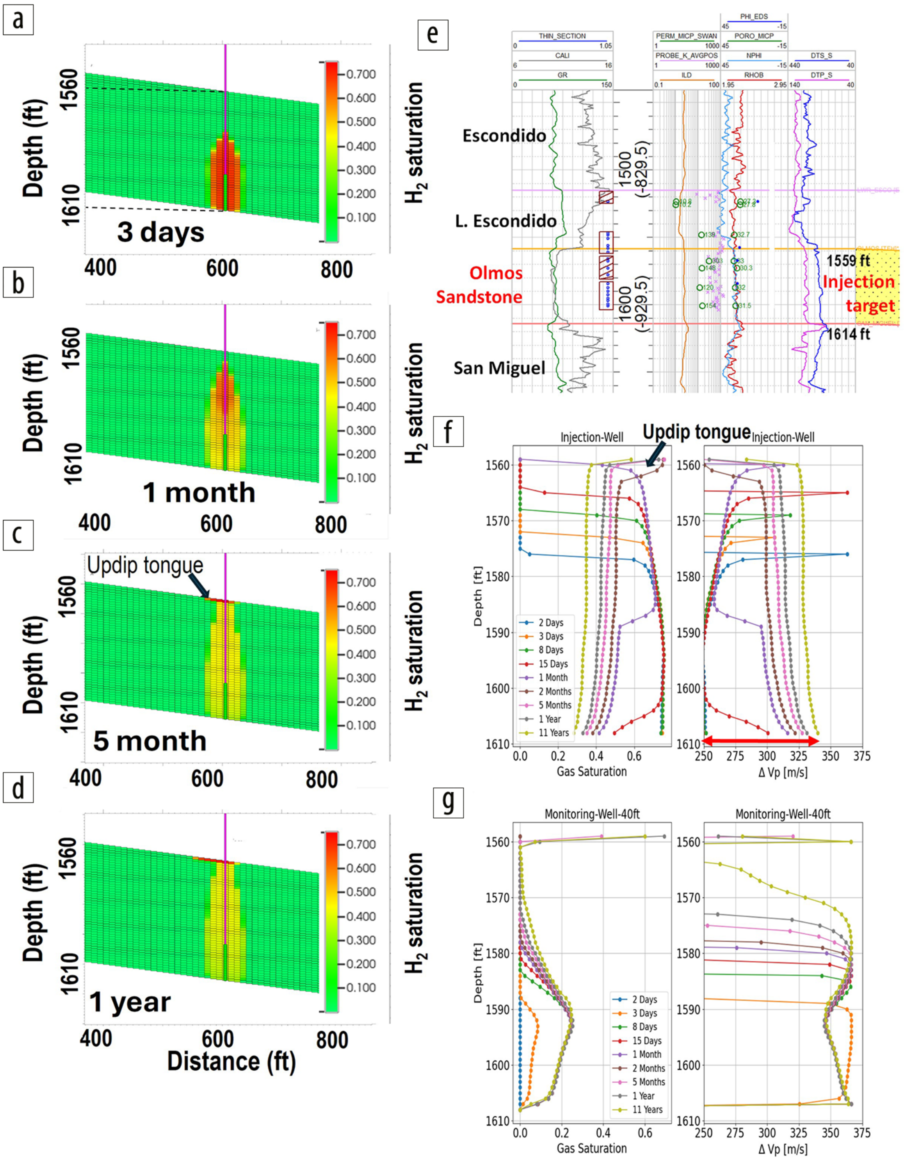

Figure 2. Reservoir simulation results and well-log overview: (a–d) vertical cross-sections of hydrogen saturation at four different time steps; (e) zoomed-in log section highlighting the seismically weak Olmos injection target (1559–1614 ft), along with overburden and underburden intervals (courtesy of Eric Radjef and the BEG/GeoH2 characterization team); (f) saturation profile and associated P-wave velocity changes along the injection well; (g) same as (f) but for the observation well located 40 ft updip. Cross sections and saturation profiles illustrate rapid upward migration of hydrogen injected in the bottom third of the reservoir, reaching the top boundary within 1 month, followed by gradual stabilization of the plume after approximately 6 months. Over time, saturation levels decrease from ~70% to ~30% as redistribution and capillary trapping dominate.

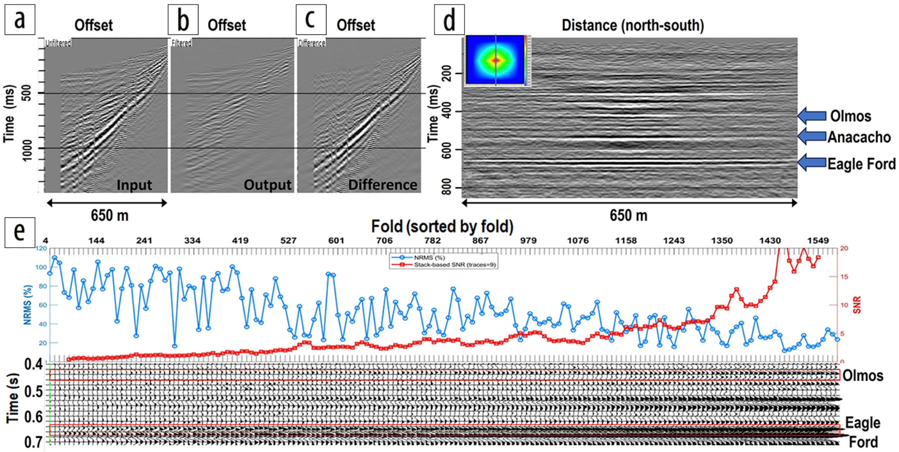

Figure 3. 3D seismic data visualization and quality assessment: (a–c) example common-shot gather acquired with a 7.5 × 7.5 m receiver grid, shown (a) before processing, (b) after NMO correction and 3D FK filtering, and (c) as a difference panel, highlighting the significant suppression of near-surface noise and improved visibility of shallow reflectors; (d) north–south vertical cross section from the intermediate 3D seismic stack showing all reflectors of interest, including the weak Olmos target at ~440 ms; (e) subset of panel (d), sorted by fold, with corresponding S/N and NRMS metrics. Note the consistent increase in S/N and decrease in NRMS with higher fold, confirming that higher-fold data yield higher-fidelity, more repeatable seismic images, validated visually by improved coherence across traces.

more subtle velocity changes, typically ~70 m/s or less (red arrow in Figure 2f). Notably, the monitor well located 40 ft updip encounters only diffuse saturation levels, below 25% even at the plume front, and with residual saturation set at 20%, shows minimal change in elastic properties over time, aside from a gradual upward change when more H_2 arrives (Figure 2g).

These results inform survey design and well instrumentation. The combination of modest injection volume and strong early-time elastic contrast may favor borehole-based methods for initial detection. The experiment includes two new wells, an injector and a monitor spaced 40–60 ft apart, each equipped with behind-casing fiber-optic sensing (DAS, DTS, DSS) and electrical resistivity tomography (ERT) arrays (Figure 1c). This setup enables multimodal acquisition of seismic, strain, thermal, and resistivity data throughout the test, with equipment examples shown in Figures 1d and 1e.

These are initial simulations for a limited injection scenario. Even at this scale, the plume shows rapid vertical ascent and strong early elastic response, suggesting hydrogen may serve as a highly visible seismic tracer, much more responsive than CO_2 in terms of velocity contrast. This enables evaluation of multiple 4D methods in a compact, cost-effective format.

The Devine monitoring design is conceived as a 4D blueprint, not limited to borehole methods, but structured to test and validate diverse approaches. These include 4D surface seismic, DAS VSP with permanent sources and receivers, crosswell seismic, and ERT. While borehole methods may offer the highest near-term sensitivity, the framework is flexible, scalable, and extensible, supporting rapid feasibility assessments for conventional and emerging monitoring technologies in a real-world, dynamic hydrogen plume setting.

Ultra-dense 3D seismic and shared-grid VSP for 4D blueprint design

Seismic characterization for the Devine hydrogen injection test was purposefully designed to support 4D monitoring. Given the weak Olmos reflector and the need to detect subtle early-time elastic changes, we pushed acquisition limits, deploying an ultra-dense 3D seismic survey and a co-located zero-offset VSP using the same shot carpet.

The 3D survey used a 7.5 × 7.5 m receiver grid (~6994 nodes) with ~1714 sources across a 650 × 650 m area, achieving an average fold of ~800 and trace densities near 30 million/km^2 (Figures 1a and 1b). This matches or exceeds modern deep-target industry standards (Lewis et al., 2021) despite the shallow target (~1600 ft). A 25-level clamped three-component (3C) geophone string in well #9 recorded the zero-offset VSP, establishing a baseline for upcoming 3D VSP analysis.

This design reflects our study's core principle: extracting maximum diagnostic value from the characterization data. By densely sampling the near surface at both the surface and in the borehole, we enable quantitative evaluation of imaging quality, repeatability, and 4D monitoring feasibility.

Initial 3D seismic assessment and fold-related repeatability trends. Figure 3a shows a representative shot gather before and after preprocessing, including 3D FK filtering that uses the dense 7.5 × 7.5 m receiver grid. Though considered geologically simple with minimal topography (Figure 4d), the prestack data reveal unexpected complexity. Reflectors are not visible in the raw gather and remain faint postprocessing, buried in the near-surface noise cone.

Despite this, dense sampling enables effective noise suppression. Figure 3d shows the resulting stacked section passing through well #9 (no surface-consistent corrections), with all major reflectors, including Olmos, visible. Reflector quality fades from the center, tracking fold reduction (Figure 1b).

Variable fold, once a limitation, now serves as a 4D design feature. By replotting the same cross section versus fold (Figure 3e), we isolate the fold's effect on signal quality. In this 1D setting, stack-based S/N rises with fold, while normalized root mean square (NRMS) drops from ~140% to ~20%, confirming better repeatability in high-fold areas.

Mapping fold footprint and near-surface thumbprints through spatially resolved S/N and NRMS analysis. To explore data quality more systematically, we extend the analysis to the full 3D stack volume. Following the approach outlined by Bakulin et al. (2024) in a desert-focused concept study, we analyze S/N and NRMS within a 40 ms window centered on the Olmos reflector (Figure 3e).

While sorting by fold is useful, expanding this analysis across the full stack risks mixing signals from distinct spatial locations, confounding fold-related effects with near-surface variability. To avoid this, we partition the volume into small, nonoverlapping tiles of ~37 × 37 m, each composed of 9 × 9 common depth points (with 3.75 × 3.75 m bin size), as shown in Figure 4b. Each tile contains ~81 traces.

NRMS is computed between each unique trace pair in a tile, typically expressed as a percentage (×100%):

$$NRMS = \frac{RMS(A-B)}{RMS(A)+RMS(B)}. \tag{1}$$

Although S/N can be estimated from trace pairs (Pevzner et al., 2011), this method is unstable at low S/N, introducing consistent overoptimistic upward bias and high variability (Bakulin et al., 2022), leading to overestimation of true signal strength. To address this, we adopt the stack-based S/N metric from the same study, which uses all traces in a tile for a more stable and reliable estimate, accurate down to –20 to –18 dB with ~70–80 traces. The data-mining workflow is as follows:

1) Fix a 40 ms window around the Olmos target for both NRMS and S/N to ensure consistency.
2) Compute a single stack-based S/N for each tile.
3) Compute NRMS between all unique trace pairs within the tile (e.g., 81 traces yield 3240 combinations), and record the mean and standard deviation.

While more refined approaches with overlapping windows are possible, we use nonoverlapping tiles for simplicity and clarity. This localized analysis preserves spatial context and supports robust estimation of repeatability and signal strength across the survey. Given the flat geology and expected reservoir homogeneity, NRMS variability across closely spaced traces (3.75 × 3.75 m grid within 37 × 37 m tiles) is not due to subsurface structure. Each tile spans only a small portion of the Fresnel zone, so variations reflect system nonrepeatability, not geologic differences.

Figure 4a shows the observed S/N map. While it generally follows the acquisition fold footprint (Figure 1b), it exhibits significantly more variability. Comparing the observed S/N (Figure 4a) with the expected S/N assuming fold as the only controlling factor (Figure 4b), we see similar large-wavelength trends, but the actual S/N displays distinct medium- and small-scale fluctuations. This mirrors findings by Bakulin et al. (2024), who observed ±10 dB S/N variations in a desert environment despite near-constant fold, driven entirely by near-surface complexity.

The NRMS map (Figure 4c) reveals localized patterns, with high-NRMS zones aligning with low-S/N areas. A key anomaly, outlined by a white dashed contour, shows both depressed S/N and elevated NRMS. This region also coincides with low amplitudes for both sources and receivers on prestack data (Figures 4e and 4f), confirming its near-surface origin. The anomaly cannot be explained by fold or geometry effects and represents a "near-surface thumbprint" — a persistent degradation tied to shallow overburden complexity. In contrast, fold-related variations are predictable "footprints" of acquisition layout.

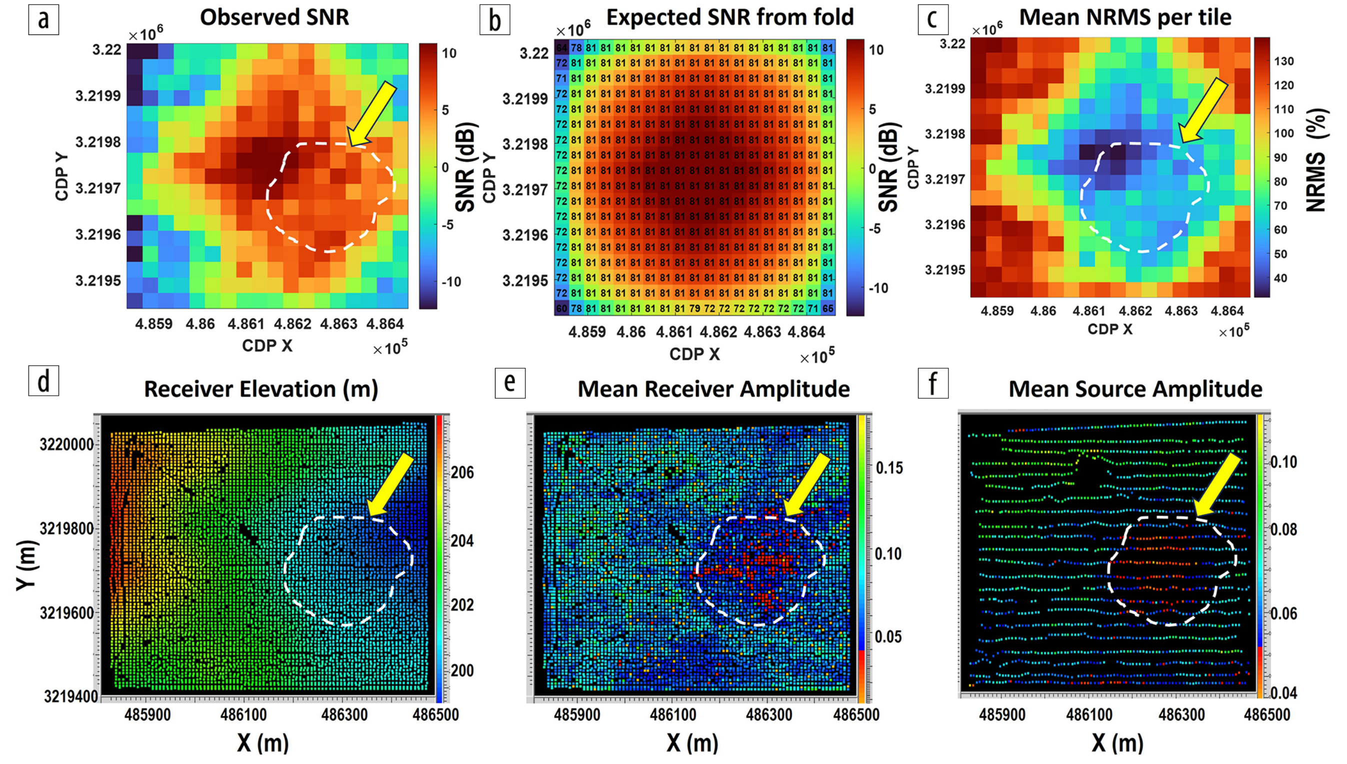

Figure 4. Analysis of S/N and NRMS across the Olmos injection target: (a) S/N map computed using a stack-based method in nonoverlapping tiles (with number of traces contributing to each tile shown in [b]); (b) expected S/N assuming an ideal case where fold is the only controlling factor; (c) NRMS map; (d) receiver elevation map; (e) and (f) mean receiver and source amplitude maps, respectively. While the observed S/N in (a) broadly follows the large-scale structure of the acquisition footprint in (b), it diverges significantly in detail due to a distinct near-surface thumbprint. For example, in the central zone (outlined with a white dashed contour), this thumbprint, unrelated to acquisition geometry, is associated with anomalously low source and receiver amplitudes (e, f) and coincides with a low-elevation region (d). The result is suppressed signal strength and reduced repeatability, manifesting as low S/N in (a) and elevated NRMS in (c), even in areas of high fold.

Here, low mean amplitudes for both sources and receivers (Figures 4e and 4f) coincide with a small topographic low (Figure 4d), and the anomalies align across maps due to the absence of surface-consistent processing. Such thumbprints are site-specific, not theoretically predictable, and must be empirically identified, making them essential considerations in 4D monitoring design.

Mining fold diversity to inform 4D survey design

The wide range of fold in the Devine 3D image presents a valuable opportunity: to extract site-specific insights into S/N and NRMS and translate them into actionable guidance for 4D survey design. Figure 5 summarizes this analysis. The left column highlights the weak Olmos injection target, while the right shows the stronger Eagle Ford reflector, used as a reference to demonstrate method robustness and result transferability.

NRMS versus fold. Figure 5a shows NRMS declining with increasing fold for Olmos, with less variability at higher fold. Using 50% NRMS as a cutoff for usable 4D signal based on synthetic modeling (Figure 6i, green curve), the mean NRMS trend offers a fast screening tool. Detailed probabilistic design curves are shown later. For now, monitoring fold must exceed ~800 for Olmos and ~200 for Eagle Ford to detect 50% NRMS signals.

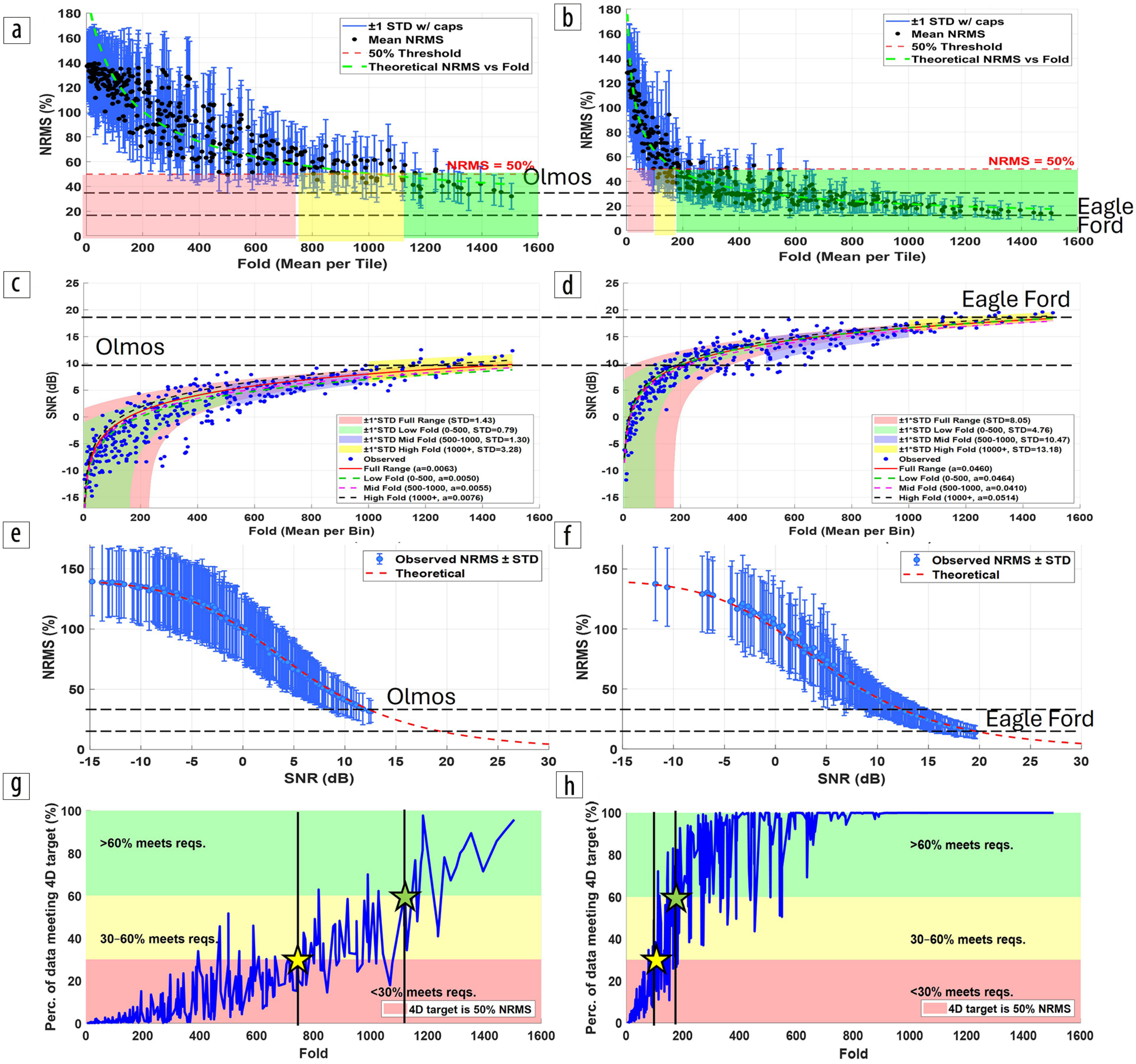

Figure 5. Summary of S/N and NRMS behavior vs fold over the weak Olmos injection target (left column) and the stronger Eagle Ford reflector (right column), using time windows from Figure 3e. Panels (a–b) show mean NRMS per tile versus fold with standard deviation bands; (c–d) display stack-based S/N versus fold with SSE model fit (equations 3-5) and uncertainty; (e–f) present NRMS versus S/N cross-plots with the theoretical curve from Equation (2); and (g–h) chart the percentage of data meeting a 4D target of 50% NRMS threshold versus fold using two design cutoffs (60% and 30% coverage). Eagle Ford exhibits consistently higher S/N (d) and lower NRMS (b) than Olmos (c and a), illustrating the relative ease of monitoring strong reflectors. Both reflectors align well with the theoretical NRMS–S/N curve (e–f), confirming that base-survey S/N is a reliable predictor of 4D performance. Variability at fixed fold stems from persistent near-surface "thumbprints." Black lines in (g–h) mark two design coverage targets (60% and 30%), which are projected onto (a–b) as fold cutoff.

Impact of signal strength. The Eagle Ford example (Figure 5b) shows that even at 200-fold, most of the data falls well below the 50% NRMS threshold. The improvement stems from stronger reflectivity, higher signal, not reduced noise. Despite experiencing the same near-surface thumbprint and noise cone, the S/N is much higher.

***S/N versus fold*.** Figures 5c and 5d show S/N versus fold trends for Olmos and Eagle Ford, following the expected √fold model, with fits across the full range (0–1600), low fold (0–500), mid fold (500–1000), and high fold (1000+). Despite similar fold values, Eagle Ford exhibits an 8–9 dB S/N uplift over Olmos, fundamentally shifting the 4D monitoring feasibility outlook, making even low-fold acquisition viable for strong reflectors, such as Eagle Ford.

Quantitative NRMS–S/N curve: A universal link between 4D performance and acquisition design. These trends are unified through the NRMS–S/N relationship (Bakulin et al., 2024), which provides a robust quantitative bridge between 4D monitoring performance and acquisition design. Unlike S/N versus fold, which typically follows a square-root trend but requires calibration, the NRMS–S/N curve is universal and requires no fitting. This makes it a powerful and practical tool. Presented here in both forward and inverse forms (rarely shown in the literature), the framework is based on energy-ratio S/N expressed in decibels, fully compatible with standard seismic processing conventions and enabling data-driven, field-relevant design decisions:

$$\text{Forward: } S/N_{lin} = \frac{2 - NRMS^2}{NRMS^2},$$

$$\text{Inverse: } NRMS = \sqrt{\frac{2}{1 + S/N_{lin}}} = \sqrt{\frac{2}{1 + 10^{\frac{S/N_{dB}}{10}}}}\,. \qquad (2)$$

This formulation resolves long-standing confusion arising from inconsistent use of amplitude versus energy-based S/N in prior work (e.g., Ronen et al., 1999; Kragh and Christie, 2002; Pevzner et al., 2011) where $S/N_{lin} = S/N^2_{amp}$.

To ground interpretation, Table 1 highlights key points along the NRMS–S/N curve: NRMS drops below 100% only when S/N exceeds 1, and achieving 0% NRMS would require infinite S/N. These values serve as practical anchors when reading NRMS–S/N plots.

Most importantly, both Olmos and Eagle Ford follow the same NRMS–S/N trend defined by equation 2, based on an uncorrelated white noise model. This matters because proxy metrics like 3DNRMS (van Gestel, 2015) help visualize relative NRMS variations but lack calibration and cannot predict absolute values or transfer across designs. In contrast, S/N is an absolute, calibrated metric. Whether derived from stacking, singular value decomposition, or correlation, S/N remains stable (Bakulin et al., 2022), making it a robust, transferable input for 4D design. With true S/N, we can quantitatively predict NRMS, not just describe relative trends. The data confirm this: Olmos (Figure 5e) shows lower S/N and higher NRMS, while Eagle Ford (Figure 5f) moves to higher S/N and lower NRMS, both aligning on the same universal curve.

Table 1. Key points along the NRMS–S/N relationship curve, illustrating interpretation thresholds.

NRMS (%)	S/N_{amp}	S/N_{lin}	S/N_{dB}
141	0	0	−∞
100	1	1	0
0	∞	∞	∞

Quantifying 4D signal magnitude using the NRMS metric

We now quantify the magnitude of the expected 4D response using the same NRMS metric applied earlier. For clarity and focus, we restrict this analysis to the near-injector location. We begin with zero-offset convolutional modeling (Figures 6a and 6b), applicable to both seismic and VSP data at the well. These are purely upgoing primary reflections, without transmission effects. This exercise shows that the initially weak Olmos reflector becomes significantly stronger within a single day, highlighting hydrogen's role as a fast-moving, high-contrast seismic tracer, far more prominent than CO_2.

Figure 6g illustrates the source of this added reflectivity: the hydrogen plume sweeps through the Olmos reservoir from bottom to top within about 30 days, progressively lowering acoustic impedance across the entire formation thickness. The corresponding 4D differences (Figure 6b) reveal a rapid emergence of signal within one day, followed by more gradual changes, a pattern confirmed in Figure 6i (blue curve), where NRMS reaches ~110% after day 1 and slowly increases to ~130% at 3 months.

These 100%–130% NRMS values must be interpreted with caution. Convolutional modeling assumes a 1D earth and infinite plume width, which inflates the 4D signal. In reality, the plume is only ~30 m wide (Figures 2a–2d and 6h), about one-tenth of the Fresnel zone at 500 m depth for a 30 Hz wavelet and 2000 m/s velocity (Hubral et al., 1993). Can such a narrow plume be detected? To answer this, we use advanced 2D FEM (Badger, 2024; Badger et al., 2024) driven by time-dependent petrophysical models from reservoir simulation (Figure 6h). To isolate the finite-plume P-wave response, we use acoustic full-waveform modeling without a free surface and adopt the acquisition geometries in Figure 6j, featuring near-zero-offset seismic and VSP centered on the injector well.

Both seismic (Figures 6c and 6d) and VSP (Figures 6e and 6f) responses show strong early 4D signals, peaking at ~80% for VSP and ~50% for seismic, with the time evolution summarized in Figure 6i. Differences arise from transmission effects and processing, as the VSP is fully processed while the seismic remains raw, but both follow a similar trend: rapid rise within about 8 days, then slower evolution. Remarkably, strong signals appear by day 1, with ~30% NRMS for seismic and ~40% for VSP, confirming the high seismic visibility of hydrogen even at small injection volume. Hydrogen's elastic response is about 20 times stronger than CO_2, reflecting the inverse ratio of their molecular weights (H_2: 2 g/mol, CO_2: 44 g/mol; B. Gurevich, personal communication). Thus, just 2 tons of H_2 may yield a signal comparable to 40 tons of CO_2. While hydrogen injection may be more expensive, it offers key advantages such as smaller required volumes, faster plume movement, and shorter monitoring durations. CO_2 has been detected at volumes as low as 38 tons at 350 m depth (Tertyshnikov et al., 2019), but hydrogen could allow for even earlier detection, making it ideal for rapid-cycle feasibility tests.

4D survey design: from feasibility to engineering

With both 4D signal (from modeling) and 4D noise (from field data) quantified, we can now shift from feasibility analysis to concrete 4D survey design. This enables a data-driven, rigorous, and transferable approach — moving beyond intuition or replication of designs from unrelated projects.

Probabilistic 4D detection design curves. Returning to Figure 5a, we can now have informed discussions with a multidisciplinary team about the feasibility of surface 4D seismic for a given injection case. Suppose we set 50% NRMS as the detectability threshold. A conservative geophysicist might demand that 60% of the data meet the requirement to ensure robust 4D interpretation, while an aggressive one may accept 30%, assuming strong well control enables broader reconstruction.

To support design choices, we extract NRMS statistics, mean and standard deviation, from the distribution of traces within each tile, across all fold levels (Figures 5a and 5b). Assuming Gaussian behavior, we compute the percentage of traces within each tile that meet the target NRMS and plot this versus fold (Figures 5g and 5h). For Olmos, reaching the 60% threshold requires ~1150-fold; relaxing to 30% lowers it to ~750. Eagle Ford meets the same thresholds at just ~180 and ~100-fold, respectively.

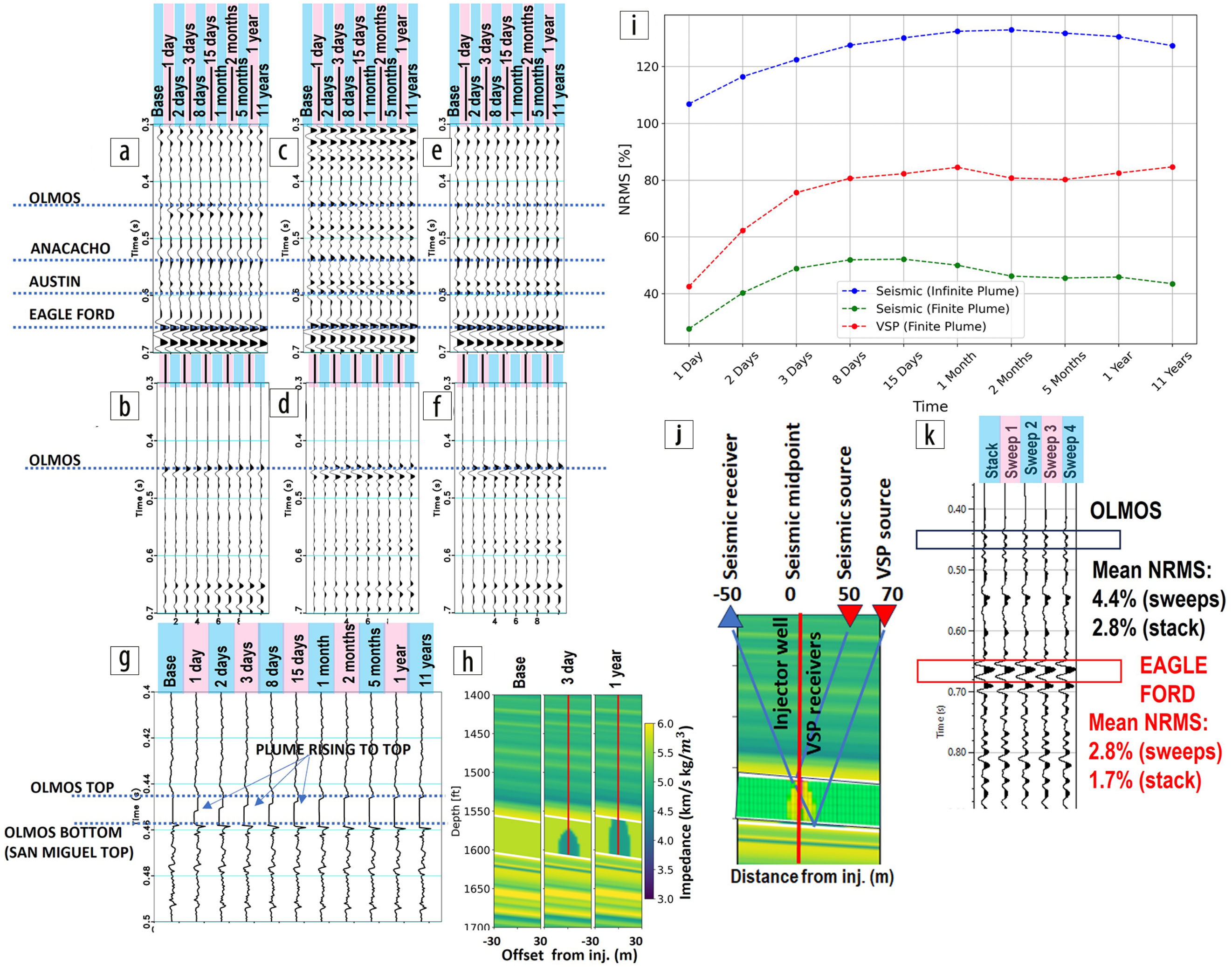

Figure 6. Quantification of 4D response from modeling surface seismic and VSP data at the well location: (a–b) Convolutional zero-offset synthetics for an unlimited plume: (a) synthetic seismograms for all time steps; (b) 4D differences between each monitor and the baseline trace, illustrating the seismic response to a laterally extensive plume. (c–d) Same as (a–b), but for a finite plume modeled using 2D finite-element simulations based on impedance models in (h) and acquisition geometry in (j). (e–f) Same as (a–b) but derived from fully processed near-zero-offset VSP responses for the finite plume. (g) Acoustic impedance profiles along the well for each time step, showing the progressive upward sweep of the Olmos reservoir by the hydrogen plume and associated decrease in acoustic impedance leading to increased reflectivity. (h) 2D acoustic impedance sections extracted along the updip direction from 3D reservoir simulations; injector is marked in red. (i) 4D NRMS over the Olmos reflector versus calendar time at the injector, measured in a 40 ms window, showing rapid signal buildup by Day 8, followed by minimal evolution. The unlimited plume case (synthetics with primaries only) yields large NRMS values (blue), while the finite plume produces a more muted response, especially in surface seismic (green), but still strong in VSP (red). (j) Acquisition geometry used for near-zero-offset seismic and VSP simulations, centered on the plume. (k) Estimated 4D noise floor from real zero-offset VSP data using four individual sweeps treated as independent time-lapse surveys: sweep-to-sweep NRMS is ~4% for the weak Olmos reflector (after processing), and roughly 2% for the stronger Eagle Ford.

By projecting these fold thresholds onto the NRMS plots (Figures 5a and 5b), we generate a decision-support chart: color-coded fold bands clearly show which fold ranges meet 4D goals and what acquisition effort is needed. This probabilistic "box test" provides a direct, data-driven way to balance monitoring value against cost.

Designing beyond fold: Linking acquisition geometry to 4D detectability. The previous analysis treated fold as the only acquisition variable, with other parameters fixed. We now generalize using the acquisition equation based on signal-strength estimate (SSE), popularized by Meunier (2011). SSE quantitatively relates amplitude-based S/N (S/N_{amp}), which in our framework is the linear amplitude S/N, to acquisition geometry and vibroseis parameters through

$$SSE(f) = Ss(f)\sqrt{TD\,RA}, \tag{3}$$

where TD is trace density (product of source density and number of receivers per shot), RA is the receiver-station area, and $Ss(f)$ is the source strength as a function of frequency f. For vibroseis acquisition, the source strength is defined as

$$Ss(f) \ = \ Pf\,D\,N_v\sqrt{\frac{L}{f_2 - f_1}}, \tag{4}$$

where Pf is the peak force, D is the drive level, N_v is the number of vibrators in the source array, L is sweep length, and f_1, f_2 are sweep limits (Meunier, 2011).

SSE is converted into theoretical energy-ratio S/N in decibels as

$$S/N_{dB}^{t} = 20\log_{10} SSE. \tag{5}$$

In our NRMS–S/N framework, SSE matches the linear amplitude S/N (S/N_{Amp}). Thus, theoretical S/N from equation 5 (S/N_{dB}^{t}) is directly compatible with our curve and usable in 4D detectability analysis. In short, $S/N_{dB}^{t} = S/N_{dB}$ from our NRMS–S/N curve. This removes ambiguity and enables direct application of acquisition parameters to 4D survey design.

Smart optimization: Enabling sparser 4D surveys without compromising performance. Suppose logistics call for a sparser 4D design, and a longer acquisition time is acceptable. If the vibrator sweep is extended by a factor of four, the source strength doubles (equation 4) and so does the *SSE* (Bakulin and Silvestrov, 2023). Because SSE scales with the square root of trace density (equation 3), TD can be reduced by a factor of four while maintaining the same SSE. This translates into an alternative 4D survey design that achieves the same NRMS and 4D performance achieved with:

- half the number of sources and half the number of receivers, or
- four times fewer sources (keeping receivers fixed), or
- four times fewer receivers (keeping sources fixed).

Equalizing monitoring performance through variable acquisition density. Once S/N is mapped and NRMS predicted, sources and receivers can be added in underperforming zones to boost S/N and reduce NRMS. The goal is a more uniform NRMS map, mitigating overburden and near-surface thumbprints through targeted acquisition. These variations can reach 10–20 dB on land (Bakulin et al., 2024) and in marine subsalt settings (van Gestel, 2015). This strategy helps equalize monitoring performance across the target. In practice, high-S/N areas are often oversampled and can be downsampled, with resources shifted to weaker zones, improving interpretability and robustness without raising cost. Thumbprints from near-surface and overburden complexity are typically fixed in time, making them ideal for one-time correction through smart acquisition. By linking monitoring performance (NRMS) with acquisition effort (via SSE–S/N), teams can make informed trade-offs, balancing cost and reliability through quantifiable, site-specific design.

VSP processing and 4D signal and noise quantification at the injection well

Zero-offset VSP processing and reflector tie. The same methodology can be applied to field VSP data from Devine. Figure 7a shows that, unlike stronger reflectors such as Eagle Ford, the weak Olmos reflector is completely obscured on the unprocessed VSP gather, buried beneath a strong train of downgoing energy. However, after standard VSP processing, it clearly emerges on the corridor stack (Figure 7d) and aligns well with the convolutional synthetic generated from the calibrated sonic log (Figure 7c).

Seismic-to-VSP alignment and bandwidth matching. A strong tie is observed between seismic and VSP (Figures 7d and 7g), with no need for phase rotation or filtering. This indicates that both processing flows preserved phase accurately and consistently. However, the seismic shows lower frequency content. Once the synthetic and corridor stack are band-passed to match the seismic bandwidth (20–60 Hz), the tie improves further (Figures 7e and 7f): the Olmos/San Miguel doublet in the full-band VSP collapses into a single-loop feature, closely matching the intermediate surface seismic (Figure 7g). This confirms the VSP's diagnostic value and compatibility with surface seismic, making it a reliable calibration reference.

4D signal quantification for near-offset VSP through modeling. The 4D signal observed in near-zero-offset VSP at the injector (Figure 6j) is significantly sharper than in surface seismic, reaching ~80% NRMS (Figure 6i, red curve). This enhanced detectability is due to the ability of VSP processing to apply array-based filtering along the borehole, removing strong downgoing energy and isolating the upgoing signal before it interacts with near-surface complexity. The temporal pattern is clear: the largest 4D change occurs within the first 8 days (reaching 80% NRMS), followed by a gradual tapering. Subsequent changes stay within a narrow band between 80% and 85%, indicating a stable signal plateau beyond the initial injection phase.

Baseline 4D noise floor estimation from field data sweep-to-sweep repeatability. The lower bound of 4D noise for VSP is estimated by treating the four individual sweeps from the zero-offset survey as independent 4D monitor surveys (Figure 6k). The resulting sweep-to-sweep NRMS is ~4.4% for the weak Olmos reflector (after processing), and about half that for the stronger Eagle Ford. Since the vibrator remained in place, without baseplate relocation, this reflects idealized, zero-time repeatability. Even submeter repositioning can degrade repeatability (Jervis et al., 2012). Still, the sweep-to-sweep NRMS suggests that small 4D signals (~ a few percent between 80% and 85%) observed after 8 days would be difficult to resolve, reinforcing the importance of early-time monitoring and highly repeatable acquisition.

4D crosswell monitoring with DAS: Resolving fine-scale plume dynamics

Reservoir simulations show plume evolution's sensitivity to reservoir properties like permeability and porosity heterogeneity, vertical-to-horizontal permeability ratio, and hydrogen–water relative permeability and capillary pressure curves, key for hydrogen storage in aquifers (Alhotan et al., 2024). High-resolution crosswell seismic and ERT between closely spaced wells could directly constrain plume geometry and infer permeability. The daisy-chained fiber-optic cable design (Figure 1c), with behind-casing DAS and ERT arrays (Figures 1d and 1e), enables focused, high-resolution monitoring. Beloborodov et al. (2024) proved the feasibility of high-frequency crosswell seismic with sparker sources (up to 1000 Hz) and DAS receivers in closely spaced wells for shallow CO_2 injection monitoring.

Modeling 4D crosswell responses with DAS. Inspired by this setup, Figure 8 shows elastic FEM for a 60 ft (18.3 m) injector–monitor pair (Figure 8a). The acquisition assumes a high-frequency sparker source (100–1000 Hz) and DAS receivers modeled as a straight fiber-optic cable with 1 m gauge length and 1 m channel spacing. The DAS response is simulated using point-strain sampling followed by integration over the gauge length, similar to Egorov et al. (2021).

The initial shot gather (Figure 8b) shows clear P- and S-wave arrivals, with bedding-parallel dimming from DAS directional sensitivity. The 4D difference at one month (Figure 8d) reveals strong changes only where raypaths intersect the plume. NRMS is near zero above but reaches 200% within the plume (Figure 8e), indicating time shifts with polarity reversal, confirmed in Figure 8i. Day-by-day analysis (not shown) captures sharp vertical and temporal variations, offering detailed insight into plume saturation and flow behavior.

Comparing modeling approaches for plume dynamics. One-dimensional convolutional modeling is well suited for surface 4D applications with vertical raypaths, while the crosswell geometry, characterized by horizontal paths, is best addressed using slowness integration along bedding-parallel trajectories to approximate traveltime shifts (orange curve, Figure 8f). These shifts capture the plume's rapid upward migration and reflect in-situ permeability. FEM serves as a benchmark; cross-correlation of synthetic direct arrivals (blue curve, Figure 8f) closely matches slowness estimates, except near the plume edges. At the reservoir top, a thin 1 ft hydrogen tongue (Figures 2c, 2d, 2f, and 2g) leads to enhanced shifts in the ray-based model (red arrow) compared to more subdued FEM responses. FEM also reveals 4D time-shift leakage into overburden zones (green arrow), a finite-frequency phenomenon not captured by ray theory. This underscores the value of full-waveform modeling for resolving subresolution plume features with crosswell DAS.

High-resolution 4D crosswell time shifts. Are we really going to chase time shifts below 1 ms? Figure 8i says yes. In high-frequency borehole data (100–1000 Hz), a 0.5 ms shift corresponds to half a wave period, clearly a strong 4D signal in crosswell geometry. This is equivalent to a 5 ms shift in conventional surface seismic (10–100 Hz), widely accepted as a robust 4D indicator. Shifts as small as 0.1 ms are not only meaningful, they are detectable, as demonstrated by Beloborodov et al. (2024) using DAS receivers and high-frequency sources in closely spaced wells.

Interpreting crosswell maps: Time shifts and NRMS. Figures 8g and 8h present traveltime shift and NRMS maps for all source–receiver pairs from a single monitor–baseline survey at 1 month, succinctly capturing the spatial detail delivered by high-resolution crosswell 4D. These maps can be inverted via traveltime or waveform tomography to infer plume shape and saturation. From a reservoir engineering standpoint, they provide two critical insights: upward plume movement directly reflects absolute permeability, while saturation evolution constrains relative permeability and residual saturation. Together, these diagnostics offer a powerful means to characterize hydrogen transport and help derisk storage strategies.

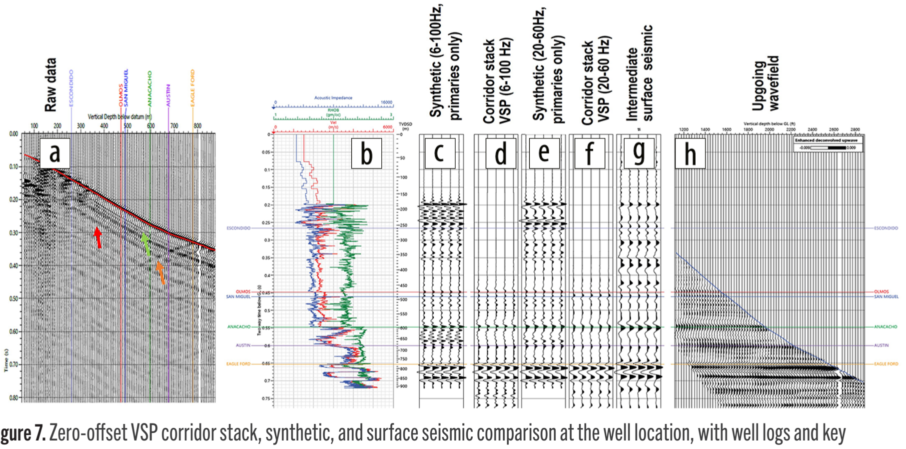

Figure 7. Zero-offset VSP corridor stack, synthetic, and surface seismic comparison at the well location, with well logs and key formation tops shown side by side: (a) Raw zero-offset VSP gather (~70 m offset) before processing, showing the prominent Eagle Ford reflector (orange arrow) while the Olmos target remains obscured (red arrow); (b) Calibrated acoustic and density logs with key stratigraphic markers; (c) Full-band convolutional synthetic from calibrated well logs; (d) Full-band VSP corridor stack; e) Band-passed (20–60 Hz) convolutional synthetic, matched to seismic bandwidth; (f) Band-passed (20–60 Hz) VSP corridor stack, matched to seismic bandwidth; (g) Intermediate surface seismic section at the well; (h) Processed and flattened upgoing VSP wavefield, input to the corridor stack. The weak Olmos reflector, initially masked in (a), becomes detectable postprocessing (h), unlike the stronger Eagle Ford. The corridor stack (d, f) ties well to the surface seismic (g), confirming stable phase handling across processing flows. Band-passing to 20–60 Hz (e, f) collapses the Olmos/San Miguel doublet into a single-loop feature, aligning with the surface seismic character (g). This confirms VSP's diagnostic value for calibration, repeatability benchmarking, and future 4D interpretation.

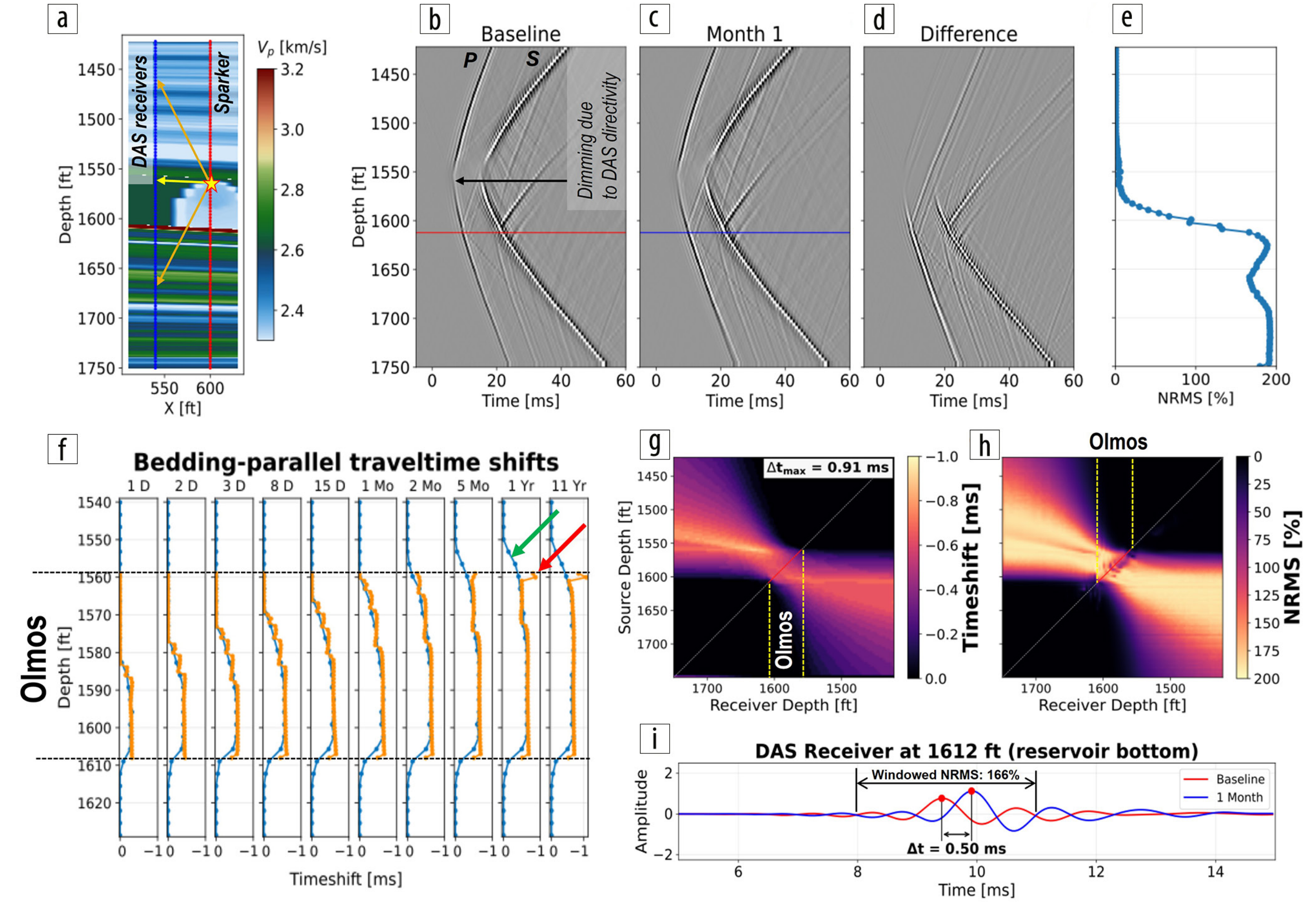

Figure 8. Quantification of 4D response for crosswell monitoring between injector and monitor wells using 2D velocity models from reservoir simulations. (a) Velocity model at 1 month, showing the plume reaching the top of the Olmos reservoir. (b–d) Common-shot gathers: (b) baseline, (c) monitor at 1 month, and (d) 4D difference, simulated using a 100–1000 Hz sparker source at 1553.2 ft (just above Olmos) and vertical DAS receivers behind casing in the monitor well (60 ft updip). (e) NRMS profile around early P-wave arrivals: near-zero NRMS above the plume rapidly jumps to nearly ~200% along intersecting paths, indicating significant time shifts leading to polarity reversal, as seen in (i). (f) Bedding-parallel traveltime shifts from analytic slowness integration (orange) versus finite-element cross-correlation of early arrivals (blue), showing excellent agreement except near the plume tongue (highlighted by arrows, discussed in text). (g) Time-shift map and (h) NRMS map across all source–receiver pairs (sources along injector, receivers along monitor), capturing rich 4D information as a function of offset and depth. (i) Zoomed waveforms at a DAS receiver at the base of Olmos (1612 ft), showing a clear 0.5 ms traveltime shift, equivalent to a half-period and triggering 166% NRMS in high-frequency crosswell data, well beyond the sensitivity of surface seismic or VSP.

Toward practical survey design: Repeatability and S/N. The next step is to evaluate 4D noise by analyzing legacy crosswell data from Devine to quantify repeatability and S/N using the same methodology. This will be supplemented by modeling the effects of nonrepeatable source positions and changes in borehole fluid (e.g., water versus hydrogen). These insights will guide optimization of survey design, including shot repeats, source type, and geometry, to maximize 4D detectability.

Conclusions

We presented a 4D survey design blueprint based on characterization data from the Devine test site, combining ultra-dense 3D seismic and VSP with FEM driven by reservoir simulations. This work supports the upcoming hydrogen injection into a shallow sandstone target at ~1500 ft (500 m).

A postage stamp–sized, densely sampled 3D seismic survey, with fold ranging from 1 to 1600, enabled direct data mining for S/N and NRMS, yielding immediate, quantitative insight into which monitoring objectives can be achieved at what acquisition effort, including associated uncertainty. These results are site-specific and cannot be derived theoretically, making this a modern-day 3D and 4D "box test."

By quantifying and linking S/N and NRMS, we established a framework equally applicable to both characterization (target S/N) and monitoring (target NRMS). With this foundation, 4D design becomes a tractable engineering task. Using the industry-standard acquisition equation, we connected NRMS targets to specific acquisition parameters, sources, receivers, arrays, sweep lengths, removing guesswork from the process.

Even in the relatively benign near-surface setting, we observed strong spatial variability in both S/N and NRMS, manifesting as persistent "near-surface thumbprints." These patterns stem from true shallow heterogeneity and cannot be predicted from geometry alone. Their impact must be quantified experimentally and mitigated through targeted, variable-density 4D acquisition.

Ultimately, enabling quantitative, data-driven 4D design is critical, not just for improving oil and gas monitoring, but even more so for gas storage and CCS, where sparse designs are often promoted as universal solutions. Yet without quantifying their effectiveness and uncertainty, the technical foundation remains weak and the defensibility under public and regulatory scrutiny questionable.

We show that hydrogen behaves as a highly visible seismic tracer, up to 20 times “brighter” than CO_2, making even small injection volumes (e.g., 2 tons) detectable via surface seismic, VSP, and crosswell DAS. Crosswell DAS offers high spatial resolution for delineating plume shape and saturation changes, helping constrain reservoir parameters such as relative permeability. The same design methodology applies across all monitoring methods, enabling direct comparison and consistent evaluation for an integrated monitoring program.

With the Devine site on track to become a shared injection monitoring laboratory for academia and industry, our goal is to establish a collaborative framework that accelerates industry advancement and fosters public learning, setting reproducible geophysical monitoring standards that are urgently needed to tackle emerging challenges like hydrogen storage, CCS, and wastewater injection, while building public trust. The methodology outlined here also lays the foundation for benchmarking 4D monitoring technologies under real-world, controlled field conditions TLE.

Acknowledgments

We thank GeoH2, TCCS, and STARR at the Bureau of Economic Geology for supporting this study. Simulations were performed on Stampede3 at the Texas Advanced Computing Center through allocation EES250046 from the Advanced Cyberinfrastructure Coordination Ecosystem: Services & Support (ACCESS) program. We thank the BEG characterization team, Bill Ambrose, Shuvajit Bhattacharya, Jerry Jense, Lucy Ko, Bob Loucks, Priyanka Periwal, and Eric Radjef, for their contributions. We also thank Harold Merry for assistance with experimental design. We thank Explor for acquiring the 3D seismic data and borehole seismic for VSP acquisition and collaboration throughout. Special thanks to Boris Gurevich for assistance with rock physics modeling, and to Roman Pevzner and Stanislav Glubokovskikh for input on experimental design. We also thank James Bailey and VSProwess for providing VSP processing software and support during analysis.

Data and materials availability

Data associated with this research are confidential and cannot be released.

Corresponding author: andrey.bakulin@beg.utexas.edu

References

Alhotan, M., M. Delshad, and K. Sepehrnoori, 2023a, Effect of grid resolution on underground hydrogen storage compositional reservoir simulation: Middle East Oil, Gas and Geosciences Show, SPE, https://doi.org/10.2118/213276-MS.

Alhotan, M., M. Delshad, and K. Sepehrnoori, 2023b, Impact of permeability heterogeneity coupled with well placement strategy on underground hydrogen storage reservoir simulation: SPE Middle East Oil, Gas and Geosciences Show, https://doi.org/10.2118/213257-MS.

Alhotan, M., M. Delshad, and K. Sepehrnoori, 2024, Sensitivity analysis of relative permeability curves in hydrogen storage reservoir simulations using Latin hypercube sampling: Presented at AGU24.

Badger, J., 2024, Scalable DPG multigrid solver with applications in high-frequency wave propagation: PhD thesis, University of Texas at Austin.

Badger, J., A. Bakulin, and S. Fomel, 2024, Scalable, efficient, and adaptive simulation of frequency-domain wave propagation: Fourth International Meeting for Applied Geoscience & Energy, SEG/AAPG, Expanded Abstracts, 1796–1800, https://doi.org/10.1190/image2024-4101625.1.

Bakulin, A., I. Silvestrov, and H. Al Salim, 2024, Predicting the success of 4D projects in complex near-surface settings: Fourth International Meeting for Applied Geoscience & Energy, SEG/AAPG, Expanded Abstracts, 2608–2612, https://doi.org/10.1190/image2024-4096030.1

Bakulin, A., I. Silvestrov, and M. Protasov, 2022, Signal-to-noise ratio computation for challenging land single-sensor seismic data: Geophysical Prospecting, **70**, no. 3, 629–638, https://doi.org/10.1111/1365-2478.13178.

Bakulin, A., and I. Silvestrov, 2023, Quantitative evaluation of 3D land acquisition geometries with arrays and single sensors: Closing the loop between acquisition and processing: The Leading Edge, **42**, no. 5, 310–320, https://doi.org/10.1190/tle42050310.1.

Beloborodov, N., K. Tertyshnikov, O. Collet, R. Isaenkov, M. Vorobev, P. Shashkin, B. Gurevich, and R. Pevzner, 2024, A field trial of cross-well seismic with DAS and a high-frequency source: Presented at the 1st ASEG DISCOVER Symposium.

Calvert, R., 2005, Insights and methods for 4D reservoir monitoring and characterization: SEG, Distinguished Instructor Series, https://doi.org/10.1190/1.9781560801696.

Devine Geophysical Test Site, n.d., https://www.beg.utexas.edu/about/facilities/dts/devine-test-site, accessed 14 January 2025.

Egorov, E., M. Charara, E. Alfataierge, and A. Bakulin, 2021, Realistic modeling of surface seismic and VSP using DAS with straight and shaped fibers of variable gauge length: First International Meeting for Applied Geoscience & Energy, SEG/APPG, Expanded Abstracts, 437–441, https://doi.org/10.1190/segam2021-3576626.1.

GeoH2, n.d., https://geoh2.beg.utexas.edu/, accessed 15 May 2025.

Hardage, B., 2004, The University of Texas Geophysical Test Site: South Texas Geological Society Bulletin, **45**, no. 3, 13–19.

Hardage, B. A., 1999, Foundation: The Leading Edge, **18**, no. 1, 16–19, https://doi.org/10.1190/tle18010016.1.

Hosseini, S. A., and J.-P. Nicot, 2016, Pressure management and plume control strategies through a brine extraction storage test at the Devine test site in Texas: U.S. Department of Energy, National Energy Technology Laboratory, Phase I Topical Report, Award No. DE-FE0026137, https://netl.doe.gov/sites/default/files/2022-06/FE0026137%20Pressure%20Management%20and%20Plume%20Control.pdf.

Hubral, P., J. Schleicher, M. Tygel, and Ch. Hanitzsch, 1993, Determination of Fresnel zones from traveltime measurements: Geophysics, **58**, no. 5, 703–712, https://doi.org/10.1190/1.1443454.

Jervis, M., A. Bakulin, R. Burnstad, C. Berron, and E. Forgues, 2012, Suitability of vibrators for time-lapse monitoring in the Middle East: 82nd Annual International Meeting, SEG, Expanded Abstracts, https://doi.org/10.1190/segam2012-0948.1.

Johnston, D., 2013, Practical applications of time-lapse seismic data: SEG, Distinguished Instructor Short Course.

Kragh, E., and P. Christie, 2002, Seismic repeatability, normalized rms, and predictability: The Leading Edge, **21**, no. 7, 640–647, https://doi.org/10.1190/1.1497316.

Lewis, A., B. Karr, R. Bianco, and S. Pollock, 2021, Illuminating fine-scale geology and creating robust seismic attributes using high trace density seismic data in the Midland Basin: Unconventional Resources

Technology Conference, 2345–2362, https://doi.org/10.15530/urtec-2021-5186.

Machado, M. V. B., M. M. Alhotan, G. R. Jerauld, M. Delshad, and K. Sepehrnoori, 2024, Fluid property characterization for underground gas storage: Journal of Clean Energy and Energy Storage, **1**, 2450004, https://doi.org/10.1142/S2811034X24500047.

Meunier, J., 2011, Seismic acquisition from yesterday to tomorrow: Distinguished Instructor Course, Distinguished Instructor Series, No. 14: SEG and EAGE.

Pevzner, R., V. Shulakova, A. Kepic, and M. Urosevic, 2011, Repeatability analysis of land time-lapse seismic data: CO2CRC Otway pilot project case study: Geophysical Prospecting, **59**, no. 1, 66–77, https://doi.org/10.1111/j.1365-2478.2010.00907.x.

Ronen, S., R. van Waard, and J. Keggin, 1999, Repeatability of sea bed multi-component data: 79th Annual International Meeting, SEG, Expanded Abstracts, 1695–1698, https://doi.org/10.1190/1.1820860.

TCCS – Texas Consortium for Computational Seismology, n.d., https://tccs.beg.utexas.edu/, accessed 15 May 2025.

Tertyshnikov, K., R. Pevzner, B. Freifeld, L. Ricard, and A. Avijegon, 2019, DAS seismic monitoring of the shallow CO_2 controlled-release experiment at the South West Hub In-Situ Laboratory: ASEG Extended Abstracts, **1**, no. 1, 1–3, https://doi.org/10.1080/22020586.2019.12072927.

van Gestel, P., 2015, 4D noise observations, Key to successful subsalt 4D: 85th Annual International Meeting, SEG, Expanded Abstracts, 5363–5367, https://doi.org/10.1190/segam2015-5847809.1.